

Tailoring Full-Spectrum Solvatofluorochromic Carbon Dots: Deciphering Tunable Multicolor Emission Mechanisms toward Advanced Photonic Cryptography

Shujing Wang, Lei Rong, Wenxuan He, Yau Kei Chan, Shuangquan Lai,* and Yi Deng*



Cite This: <https://doi.org/10.1021/acs.nanolett.5c05189>



Read Online

ACCESS |



Metrics & More



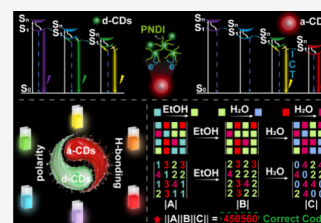
Article Recommendations



Supporting Information

ABSTRACT: The growing demand for high-security optical encryption and anticounterfeiting technologies necessitates the development of full-spectrum multimodal luminescence materials and strategies. However, integrating full-color emission and multilevel response modes within a single system remains challenging. Herein, a facile one-pot solvothermal strategy is developed to tailor two distinct carbon dots (CDs), dispersed CDs (d-CDs) and aggregated CDs (a-CDs), exhibiting full-spectrum multimodal photoluminescence. Systematic investigations reveal that the multicolor emission originates from intrinsic, deep defective, and surface states in both d-CDs and a-CDs, while a-CDs uniquely exhibit an additional molecular state via intramolecular charge transfer. Remarkably, the photoluminescence behavior can be dynamically modulated by solvent polarity and hydrogen bonding, enabling on-demand full-spectrum photoluminescence responses. With the leverage of these exceptional full-spectrum solvatofluorochromic properties, advanced encryption platforms with high-level security are demonstrated. This work not only deciphers the multicolor emission origins and solvatofluorochromic mechanisms of CDs but also offers new perspectives for designing intelligent materials for optical security applications.

KEYWORDS: carbon dots, full-spectrum multimodal photoluminescence, fluorescence origins, solvatofluorochromic mechanisms, photonic cryptography



Information leakage and data falsification have emerged as global challenges with the boom of modern technology, exerting profound threats to social stability and economic development.^{1–3} According to Zion Market Research, the global information protection market is forecast to reach USD 208.71 billion by 2026,⁴ underscoring the paramount necessity for developing novel encryption and anticounterfeiting materials and technologies. Specifically, owing to their merits of chromatic variety, visual readability, and distinctive fluorescence concealment, stimuli-responsive luminescent materials have garnered considerable attention in security applications.^{5–7} Despite pioneering studies that have played a pivotal role in the leapfrog development of smart materials and their expansion into advanced photonic cryptography systems, several formidable tasks still need to be resolved. First, due to the lack of clear theoretical and design guidance, the development of stimuli-responsive luminescent materials meets a tremendous challenge to realize the full-spectrum multimodal emission, which can convey richer data and enable seamless editing. Meanwhile, owing to the complexity of the luminescent mechanism, the integration of full-color emission and multilevel response mode in one multistimuli responsive system, which can be regarded as an effective strategy to prevent the encryption of information or data from being stolen, mimicked, or forged, remains a persistent obstacle.⁸ However, the majority of existing materials remain constrained by limited emission colors and decryptable “static” information or patterns, resulting in low information capacity

and susceptibility to forgery. Consequently, to satisfy the complex scenarios and high-security level of optical encryption systems, there is an urgent demand for tailoring innovative stimuli-responsive luminescent materials featuring full-spectrum multimodal emission and multilevel fluorescence response capabilities.

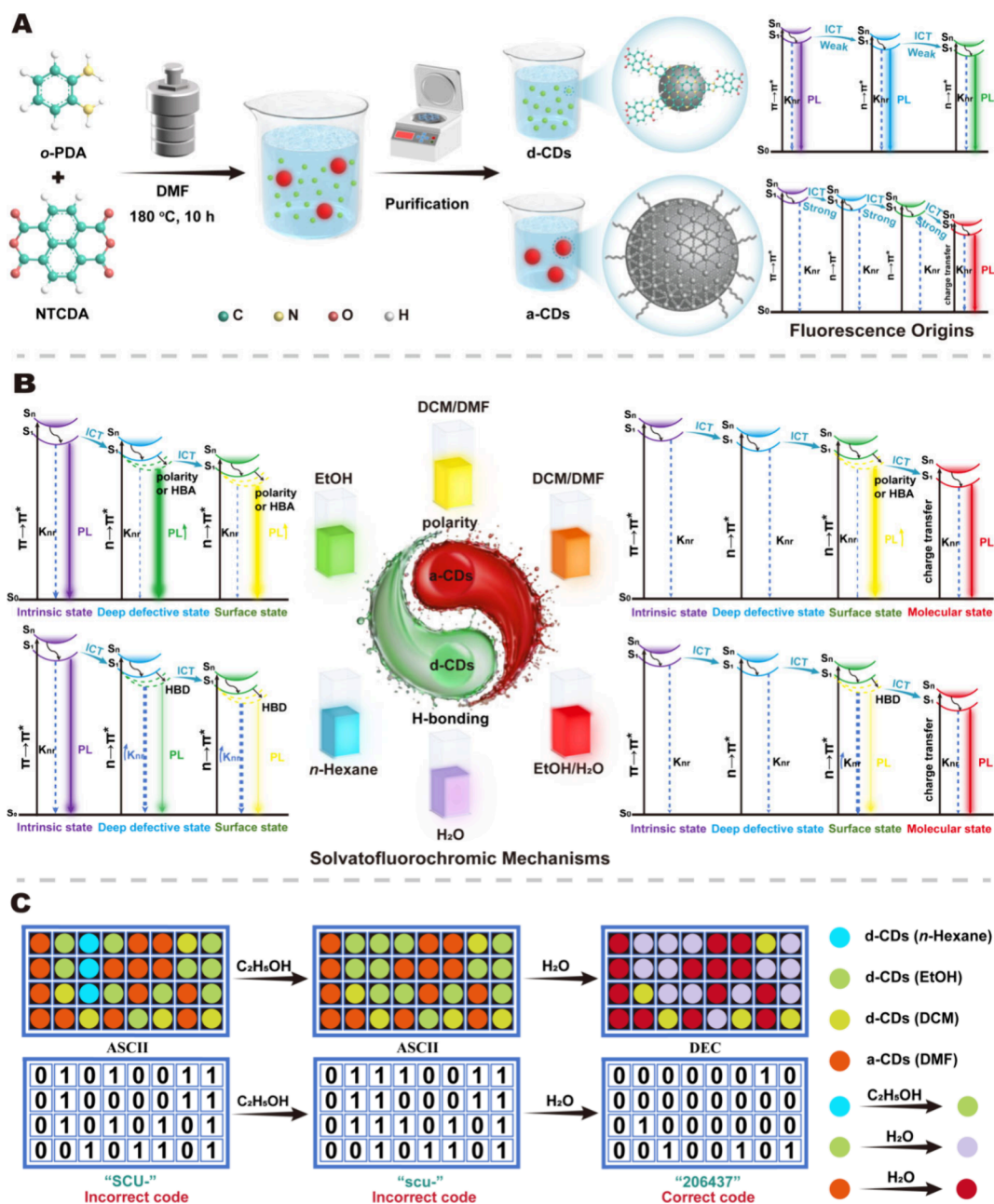
Carbon dots (CDs), as a class of burgeoning zero-dimensional nanoluminescence material, have attracted widespread attention due to their facile synthesis and remarkable fluorescence properties.^{9,10} Recently, CDs have witnessed rapid development and shown great application potential for optical encryption and anticounterfeiting technology owing to their controllable structures and adjustable photoluminescence (PL).^{4,11} Nevertheless, the underlying mechanisms governing their fluorescence color regulation remain controversial, significantly impeding the realization of full-spectrum multimodal PL for further advancement of CDs. A multitude of factors have been proposed to account for the fluorescent behaviors of CDs, with surface state emission considered a key mechanism for color modulation.¹²

Received: October 16, 2025

Revised: December 9, 2025

Accepted: December 10, 2025

Scheme 1. Schematic Illustration of the (A) Synthesis Process and Fluorescence Origins, (B) Solvatofluorochromic Mechanisms, and (C) Dynamic Encryption and Anti-counterfeiting Applications of d-CDs and a-CDs



Existing research investigated the impacts of surface passivation on the fluorescence of CDs and proposed a surface energy trap-controlled fluorescence mechanism.^{13,14} Moreover, it has been indicated that the synergistic effect between the surface state and the carbon-core state contributes to the multicolor fluorescence of CDs.^{15,16} Interestingly, solvents can alter the surface states of CDs, which is attributed to the interactions between solvent molecules and functional groups on the CDs' surface, consequently affecting their fluorescence emission colors.¹⁷ Therefore, it is feasible to achieve dynamic multicolor to even full-spectrum fluorescence modulation by leveraging the solvent-responsive properties of CDs. However, the ambiguous multicolor fluorescence origins and elusive solvatofluorochromic mechanisms of the CDs impede their further progress in advanced encryption and anticounterfeiting applications.

Herein, we report a one-pot solvothermal synthesis and separation of two distinct solvent-responsive luminescent CDs [dispersed CDs (d-CDs), aggregated CDs (a-CDs)] from *o*-phenylenediamine (*o*-PDA) and 1,4,5,8-naphthalenetetracarboxylic dianhydride (NTCDA) under identical reaction conditions. Systematic characterizations revealed three coexisting emission states in d-CDs (intrinsic, deep defective, and surface states), while a-CDs exhibited an additional molecular state emission due to intramolecular charge transfer (ICT) between d-CDs and poly(naphthalenediimide) (PNDI)-bridged polymeric structure (Scheme 1A). This work first elucidates the decisive role of diverse emission states in multicolor PL tuning. Based on the newly elucidated PL origins, we investigated solvent effects by varying polarity and hydrogen-bonding through comparative experiments to achieve dynamic

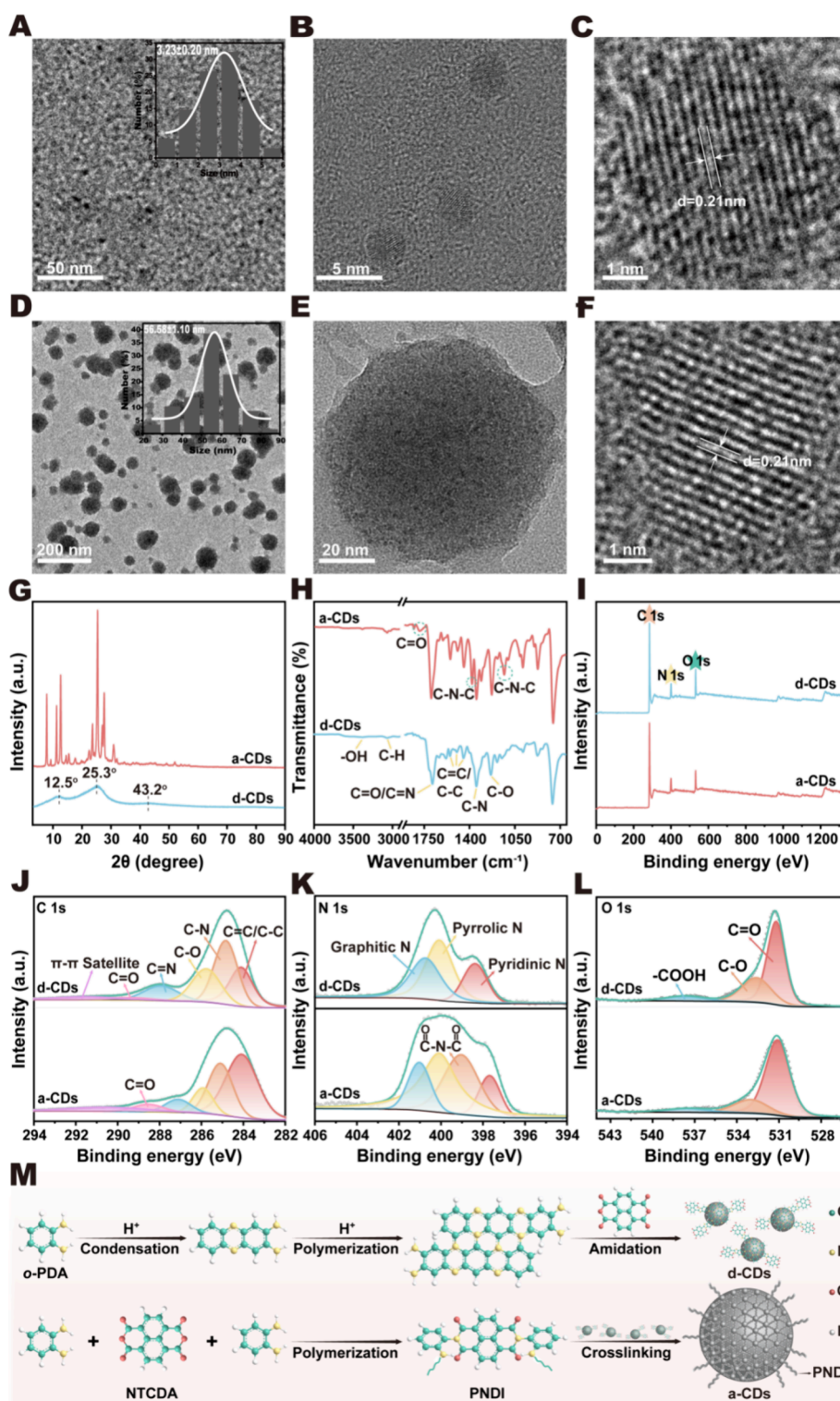


Figure 1. Characterization and synthesis of d-CDs and a-CDs. (A and B) TEM and (C) HRTEM images of d-CDs. (D and E) TEM and (F) HRTEM images of a-CDs. (G) XRD patterns of d-CDs and a-CDs. (H) FTIR spectra of d-CDs and a-CDs. (I) XPS survey spectra and (J) C 1s, (K) N 1s, and (L) O 1s of d-CDs and a-CDs. (M) Schematic illustration of the synthetic pathways for d-CDs and a-CDs.

full-spectrum multimodal PL. The solvatofluorochromic mechanisms were found to exclusively operate on the deep defective, surface, and molecular state. Intriguingly, enhanced polarity and hydrogen-bonding (DCM/DMF as acceptors) boost emission by suppressing non-radiative decays, whereas hydrogen-bonding (EtOH/H₂O as donors) promotes non-radiative pathways, leading to fluorescence quenching of all three states (Scheme

1B). Furthermore, leveraging the exceptional full-spectrum fluorescence and solvatofluorochromism of the tailored CDs, we successfully developed various advanced encryption and anticounterfeiting systems by integrating with logic gates, mathematical algorithms, and color-coding technologies (Scheme 1C). This demonstration opens new avenues for smart optical security applications.

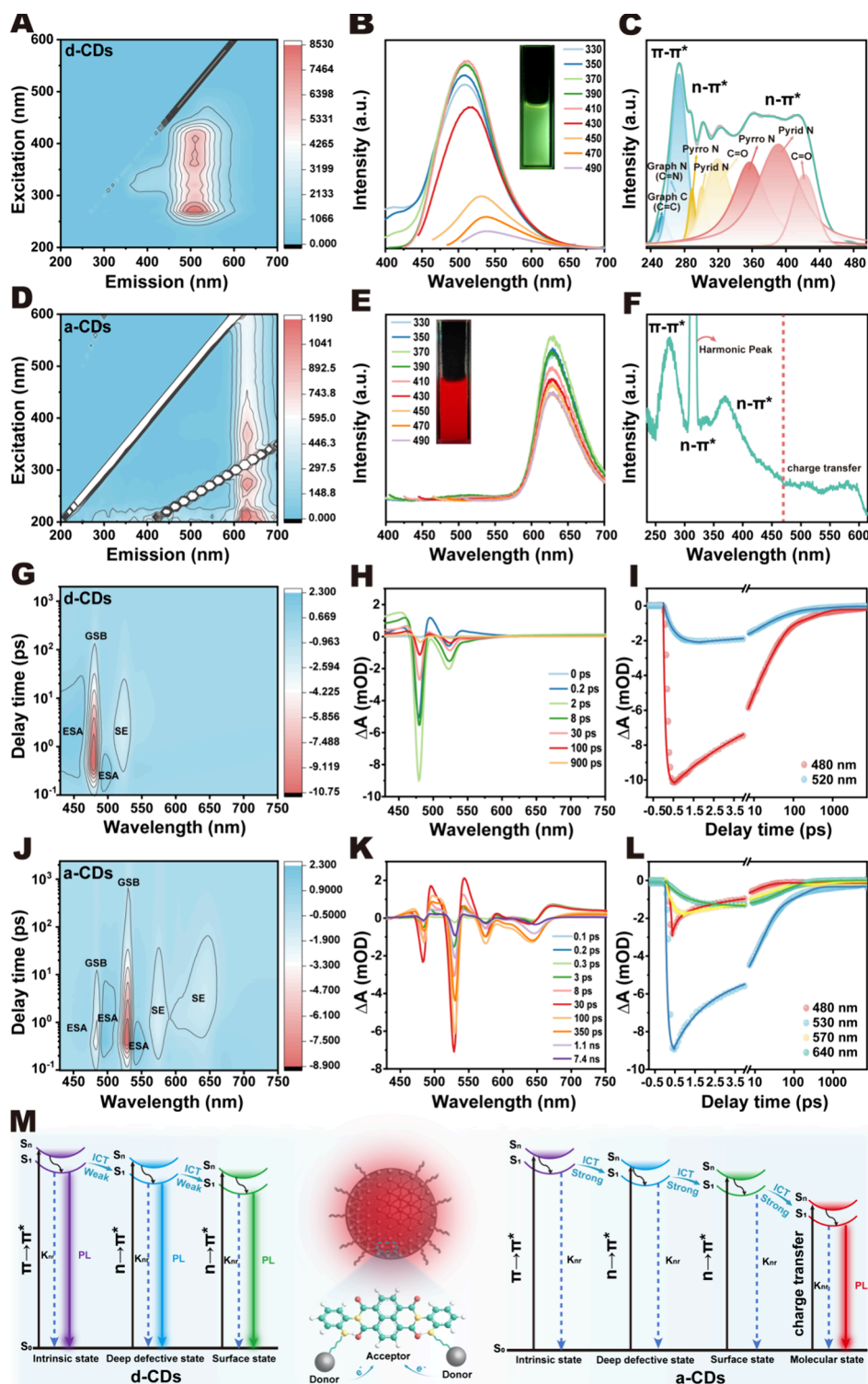


Figure 2. Photoluminescence performance, TA spectroscopy, and photoluminescence mechanisms of d-CDs and a-CDs. (A) Excitation–emission maps, (B) emission spectra under different excitation wavelengths, and (C) excitation spectra at 510 nm emission wavelength for d-CDs in anhydrous EtOH. (D) Excitation–emission maps, (E) emission spectra under different excitation wavelengths, and (F) excitation spectra at 630 nm emission wavelength for a-CDs in anhydrous EtOH. TA spectra of (G) d-CDs and (J) a-CDs. TA spectra of (H) d-CDs and (K) a-CDs at the different delay times. Kinetic traces of (I) d-CDs and (L) a-CDs at different probe wavelengths. (M) Schematic diagrams of the photoluminescence mechanisms of d-CDs and a-CDs, respectively.

Transmission electron microscope (TEM) images (Figure 1A and B) showed that the d-CDs were homogeneous, well-dispersed nanodots with a size of 3.23 ± 0.20 nm. The high-resolution TEM (HRTEM) image of d-CDs (Figure 1C) revealed a lattice spacing of 0.21 nm, corresponding to the (100)

plane of the graphitic carbon structure.^{18,19} Contrastively, a-CDs were aggregated particles with an average size of 56.58 nm (Figure 1D). The enlarged image (Figure 1E) showed numerous CDs embedded within, and the 0.21 nm lattice spacing in HRTEM (Figure 1F) confirmed they were d-CDs. Since diimide

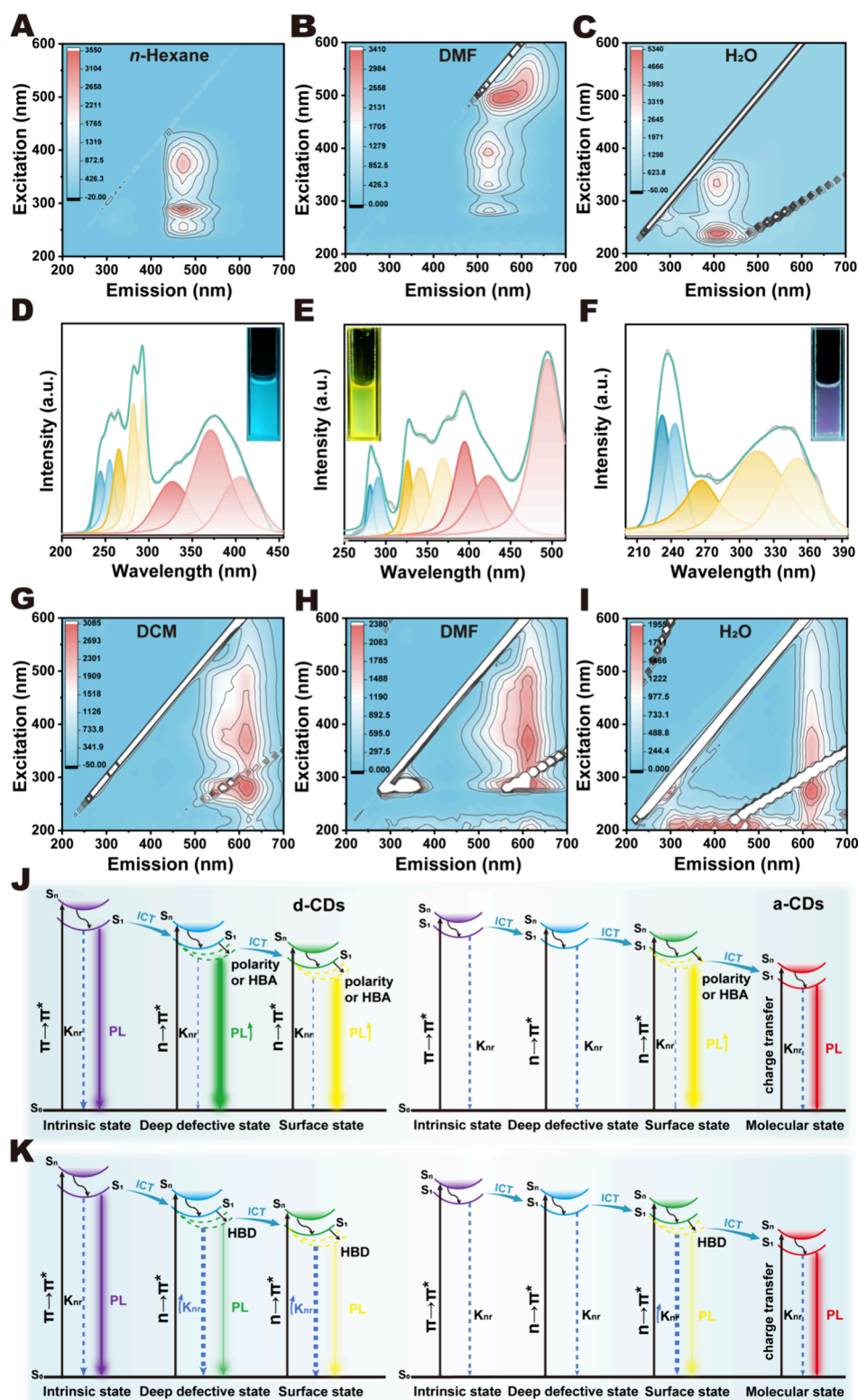


Figure 3. Photoluminescence performance and related solvatofluorochromic mechanisms of d-CDs and a-CDs in different solvents. Excitation–emission maps of d-CDs in (A) *n*-hexane, (B) DMF, and (C) H₂O. Excitation spectra of d-CDs in (D) *n*-hexane, (E) DMF, and (F) H₂O at 470, 530, and 420 nm emission wavelength, respectively. Excitation–emission maps of a-CDs in (G) DCM, (H) DMF, and (I) H₂O. Proposed solvatofluorochromic mechanisms: the effect of (J) solvent polarity and (K) hydrogen bonding on the photoluminescence performance of d-CDs and a-CDs.

polymer could be formed after polymerization of dianhydride and diamine molecules, the formation of a-CDs could be attributed to the d-CDs being cross-linked and embedded by the polymer chains.^{20,21}

As presented in Figure 1G, the X-ray diffraction (XRD) results revealed that d-CDs exhibit three broad diffraction peaks at 12.5°, 25.3°, and 43.2°, corresponding to *d* spacings of 0.71, 0.35, and 0.21 nm, which could be attributed to the (004),

(002), and (100) planes of graphitic carbon.²² However, the XRD pattern of a-CDs exhibited not only a predominant peak at 25.3° but also numerous sharp diffraction peaks, which resembled those of some reported polymer dots with polymer structures.¹⁸ The results further proved the composite structure of a-CDs, comprising carbon domains and polymeric constituents. Subsequently, the structures of CDs were characterized using Fourier transform infrared (FTIR) spectroscopy (Figure 1H). Notably, due to the vibrational coupling of the imide ($\text{O}=\text{C}-\text{N}-\text{C}=\text{O}$) structure in a-CDs, not only a $\text{C}=\text{O}$ peak at 1695 cm^{-1} but also an additional asymmetric stretching vibration peak at 1785 cm^{-1} is observed. X-ray photoelectron spectroscopy (XPS) results proved that both kinds of CDs consist of C, N, and O atoms (Figure 1I). Notably, in the high-resolution XPS spectra (Figure 1J), the $\text{C}=\text{O}$ peak in a-CDs exhibited significantly greater intensity, which arose from the introduced imide groups within the polymeric structure. In Figure 1K, a-CDs demonstrated an additional peak at 399.1 eV ($\text{O}=\text{C}-\text{N}-\text{C}=\text{O}$),²³ proving the structural differences between these two kinds of CDs. Meanwhile, the amount of $\text{C}=\text{O}$ bond relative to $\text{C}-\text{O}$ bond for a-CDs was significantly increased compared with d-CDs (Figure 1L and Table S1).

Based on the above results, the formation mechanism of CDs could be illustrated as shown in Figure 1M. During the solvothermal reaction process, NTCDA could promote the protonation and subsequent polymerization of *o*-PDA, facilitating the longitudinal growth ($-4045.23\text{ kJ mol}^{-1}$) rather than lateral growth ($+1.92\text{ kJ mol}^{-1}$) to obtain wide conjugated planar structures.²⁴ The exposed amino groups on these planar segments then underwent acylation and condensation with NTCDA, ultimately yielding planar molecular units containing abundant functional groups. These units subsequently tended to aggregate into spherical d-CDs. Since a-CDs were found to consist of nanodots and polymeric constituents, the aggregates thus could be attributed to the cross-linking of multiple d-CDs by the polymer chains, which were formed by the polymerization of residual *o*-PDA and NTCDA molecules. Molecular modeling confirmed that the PNDI exhibited non π -conjugation, indicating their negligible contribution to the conjugate structure of d-CDs.

To verify the aforementioned conclusions, the PL performance of d-CDs/a-CDs in EtOH was characterized. As illustrated in Figure 2A, the excitation–emission matrix (EEM) spectrum of d-CDs in EtOH demonstrated multiple PL emission centers, which could be attributed to the emission of the intrinsic, deep defective, and surface states, respectively.²⁵ Under 365 nm excitation, the solution demonstrated green fluorescence (Figure 2B). To explore the PL origins of the d-CDs, the excitation spectrum of d-CDs was analyzed and deconvoluted into eight Gaussian peaks (Figure 2C): (1) 253.4 and 273.4 nm, intrinsic state; (2) 288.8, 300.6, and 319.2 nm, deep defective state; and (3) 357.0, 391.0, and 421.8 nm, surface state.

Compared to d-CDs, a-CDs exhibited significant alterations in their luminescence properties. The EEM spectrum (Figure 2D) revealed that the maximum emission center migrated from 510 nm for d-CDs to 630 nm for a-CDs, along with reduced fluorescence intensity. Moreover, the emission spectrum (Figure 2E) exhibited excitation-independent emission characteristics with a fixed wavelength at 630 nm, displaying red fluorescence under UV and visible light illumination. The PLE spectrum (Figure 2F) of a-CDs demonstrated that the fluorescence emission also exhibited intrinsic, deep defective, and surface states (with the deep defect state peak obscured by

the harmonic peak at 315 nm). Notably, compared to d-CDs, a new broad peak emerged between 470 and 615 nm, originating from CT.

The polymer bridges structure in a-CDs, which was essentially a PNDI core conjugated with two strong electron-withdrawing imide groups ($-\text{CO}-\text{N}-\text{CO}-$).²⁶ The strong electron-withdrawing inductive and conjugative effects of the imide groups significantly lowered the system's LUMO energy level, facilitating electron acceptance.^{27–29} Specifically, d-CDs acted as the electron donors, forming an alternating D–A–D–A stacking structure. The broad excitation band spanning 470–615 nm in Figure 2F originated from surface state CT, referred to as the molecular state, and caused the fluorescence emission in a-CDs to shift from surface state to molecular state dominance, resulting in a red shift of the fluorescence peak and a decrease in fluorescence intensity.^{30–33}

To validate the CT mechanism, femtosecond transient absorption (TA) measurements were conducted. For d-CDs (Figure 2G), the initial signal growth was proposed to result from electron relaxation from upper to lowest excited states via phonon scattering in the hybridized carbon core.²⁴ For a-CDs (Figure 2J), molecular state GSB exhibited higher intensity and longer delay time, indicating CT from surface to molecular state. The SE signals of surface state appeared at 570 nm but disappeared in the PL spectrum of a-CDs, further confirming the CT process. Moreover, the spectral evolution of the CDs was depicted at different delays (Figure 2H and K). Meanwhile, both d-CDs (520 nm SE) and a-CDs (570/640 nm SE) displayed triple-exponential decays (Figure 2I and L and Tables S3 and S4). The three lifetimes in d-CDs were attributed to non-radiative recombination, trapped charges, and emission,³⁴ while the longer lifetime at 640 nm in a-CDs signified the CT from surface to molecular state.³⁵

The results show CDs exhibit distinct PL mechanisms (Figure 2M). In d-CDs, light excites molecules to S_n states, which relax to S_1 and emit fluorescence ($S_1 \rightarrow S_0$) through combined intrinsic, deep defective, and surface states with weak ICT, while some energy is lost via non-radiative (K_{nr}). In a-CDs, charges transfer sequentially from intrinsic to deep defective state, then to surface state, then fully to molecular state, quenching the first three states' fluorescence, leaving only red molecular-state emission.

The PL properties of d-CDs dispersed in nonpolar, aprotic *n*-hexane were systematically investigated first. According to the EEM spectrum (Figure 3A), the solution demonstrated multiple PL emission centers with the maximum one at 470 nm. The emission spectra displayed intrinsic (445 nm), deep defective (470 nm), and surface states (500 nm), respectively (Figure S13). In DCM (moderately polar, aprotic) and DMF (highly polar, aprotic), multiple fluorescence emission centers were also observed (Figure 3B and Figure S14A). Furthermore, the d-CDs exhibited a maximum emission center at 420 nm in H_2O (strongly polar, protic), which fell within the violet light region (Figure 3C). These results were further corroborated by the fluorescence emission spectra (Figure S15). To elucidate the underlying mechanisms, Gaussian deconvolution analysis was performed on the excitation spectra of d-CDs solutions. In *n*-hexane, DCM, and DMF, eight constituent peaks were consistently identified (Figure 3D and E and Figure S14B), matching the quantity observed in EtOH. This confirmed the coexistence of intrinsic, deep defective, and surface states. However, both peak positions and relative intensities exhibited solvent-dependent variations.

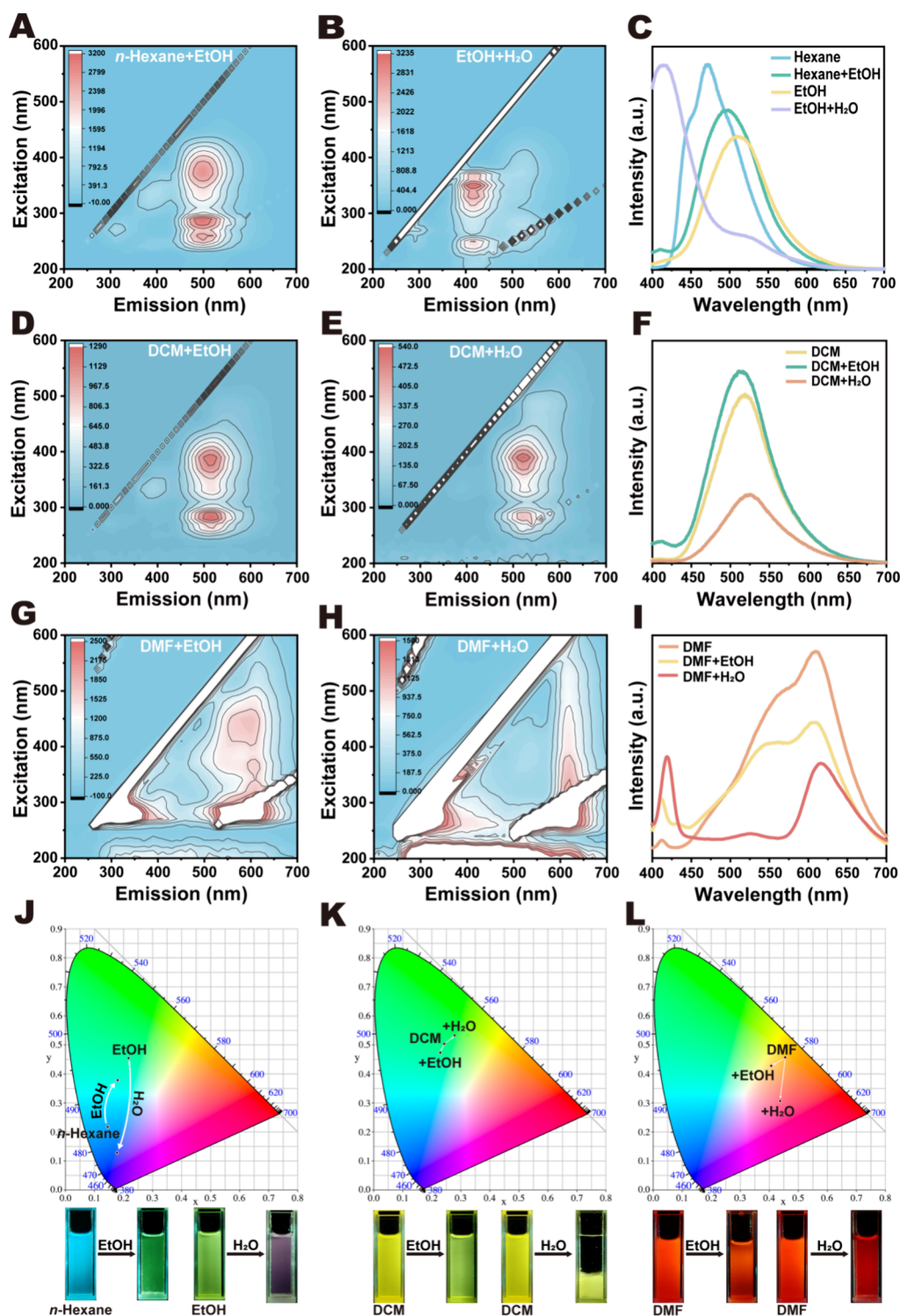


Figure 4. Solvent-responsive properties of d-CDs and a-CDs in different solvents. EEM spectra of the solution after the addition of (A) EtOH in *n*-hexane and (B) H₂O in EtOH of d-CDs. EEM spectra of the solution after the addition of (D) EtOH and (E) H₂O in DCM of d-CDs, respectively. EEM spectra of the solution after the addition of (G) EtOH and (H) H₂O in DMF of a-CDs, respectively. (C, F, and I) Emission spectra of each solution under 365 nm excitation. (J–L) Changes in CIE coordinates caused by solvent responsiveness and the optical images of the solution.

As hydrogen bond acceptors (HBAs),³⁶ DCM and DMF interact strongly with the outermost –COOH groups on d-CDs, enhancing the corresponding deconvoluted peak intensity. In contrast, surface-state pyrrolic N experienced steric hindrance, leading to weaker hydrogen bonding. Deprotonation of d-CDs reduced the energy gap between intrinsic and deep defective/surface states while decreasing non-radiative energy dissipa-

tion,³⁷ thereby enhancing PL intensity and shifting fluorescence dominance to deep defective and surface states. Additionally, increasing solvent polarity further promoted emission via dipole stabilization of the excited state, reducing *S*₁ energy and causing a red shift.^{38,39} Increased polarity suppressed non-radiative transitions and enhanced emission from both deep defective and

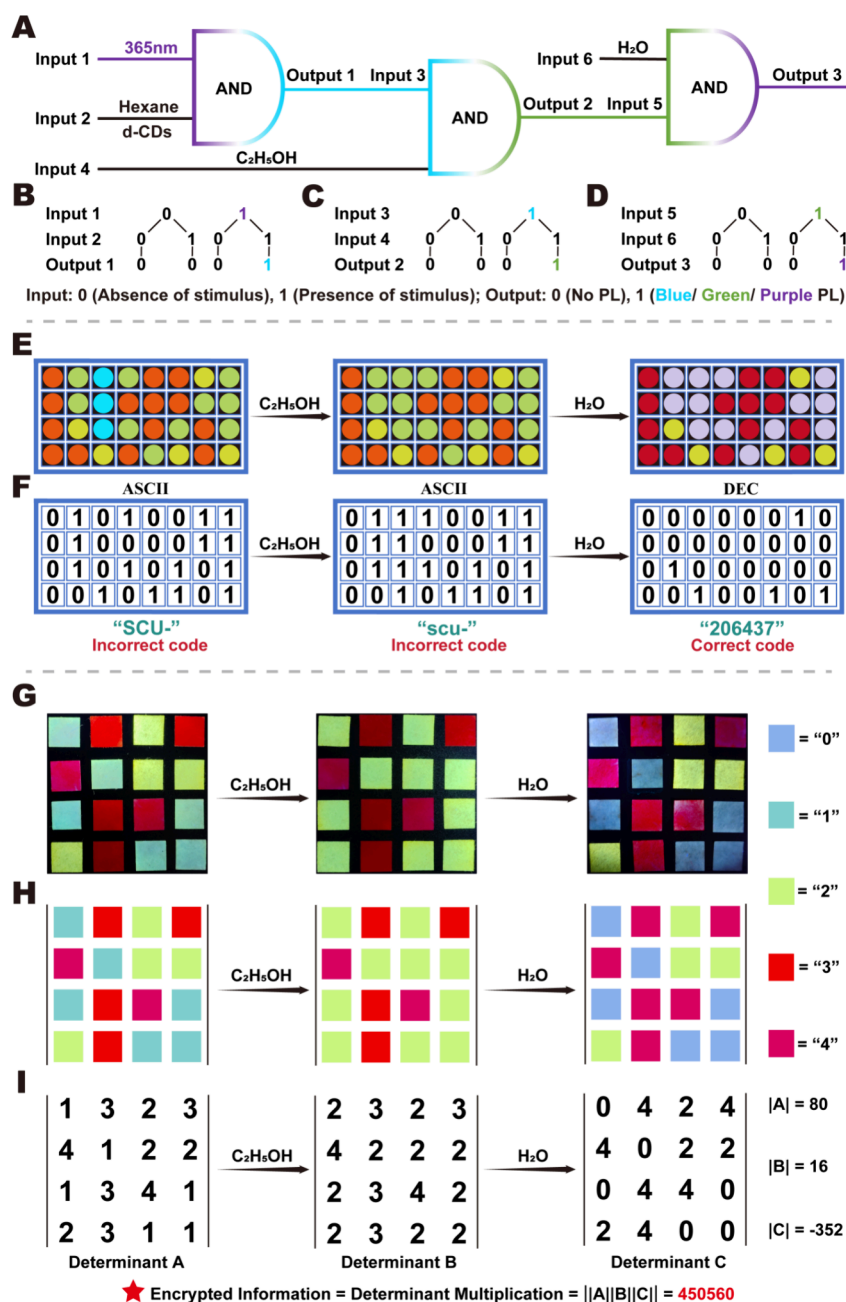


Figure 5. Dynamic encryption and anticounterfeiting applications of d-CDs and a-CDs. (A) Physical electronic representation of integrated logic gates. The tree diagram of d-CDs-encrypted (B) output 1, (C) output 2, and (D) output 3. (E) Schematic diagram of (4 × 8) matrix evolution and (F) passwords variation during binary-decimal conversion. (G) Photographic documentation, (H) operational schematic, and (I) corresponding calculations of the fourth-order determinant for advanced dynamic data encryption.

surface states. Therefore, polarity and HBA ability synergistically intensified fluorescence, yielding similar emission profiles.

Furthermore, the d-CDs in hydrogen bond donors (HBDs) appearing a significant blue shift compared to in HBA.^{36,40} In EtOH, weaker hydrogen bonding incompletely suppressed surface-state emission. However, in H₂O, strong hydrogen bonding passivated deep defective and surface states while promoting non-radiative transitions. Excessive solvent polarity further quenched surface emission via opening additional non-radiative relaxation channels.⁴¹ Consequently, fluorescence originated mainly from the intrinsic state, with minor deep defective state contribution, resulting in a violet-emitting blue shift (Figure 3F).

With ICT, a-CDs displayed exclusively surface-state and molecular-state fluorescence. In aprotic solvents (DCM and DMF), EEM spectra displayed multiple emission centers (Figure 3G and H), with a shoulder peak at 570 nm (assigned to surface-state emission via TA) and a dominant peak at 610 nm in emission spectra (Figure S16A and B). Weak hydrogen bonding in these solvents prevented complete quenching of surface-state emission, which diminished under longer excitation (≥ 510 nm), leaving only molecular-state emission. Increasing solvent polarity red-shifted surface-state emission, weakening the 570 nm shoulder in DMF relative to DCM. However, solvent polarity had negligible effect on molecular-state emission (~ 610 nm). In contrast, strong hydrogen

bonding in H₂O and EtOH fully quenched surface-state emission, yielding single molecular-state-dominated emission at 620 nm (Figure 3I and Figure S16C). Different solvents' excitation spectra consistently revealed peaks corresponding to intrinsic, deep defective (partially overlapped by harmonic peak), surface, and CT-induced molecular states (Figure S17A–C).

Figure 3J and K illustrates solvent polarity and hydrogen bonding effects on CDs. For d-CDs, HBA and higher polarity enhanced deep defective/surface state PL while suppressing K_{nr} without affecting intrinsic state emission. HBD had the opposite effect: stronger hydrogen bonding promoted K_{nr} and quenched deep defective/surface state PL. For a-CDs, intrinsic and deep defective states were quenched by strong ICT, leaving only surface/molecular state emission. Solvents primarily impacted the surface state, with minimal effects on the molecular state, polarity/HBA enhanced PL and reduced K_{nr} , while HBD increased K_{nr} and quenched PL. Thus, CDs' solvatofluorochromism was jointly controlled by polarity and hydrogen bonding.

Inspired by the full-spectrum solvatofluorochromic characteristic of CDs (Figure S23), we investigated their solvent-responsive properties. Adding EtOH to d-CDs in *n*-hexane caused a red shift (470 → 500 nm) and color change (blue → green) due to increased polarity, enhancing deep defective/surface state emission (Figures 3A and 4A, C, and J). Subsequent H₂O addition quenched green emission with a 95 nm blue shift (510 → 415 nm) as HBD dominance suppressed deep defective/surface state, leaving intrinsic state emission (purple fluorescence) (Figures 2A and 4B, C, and J). Adding EtOH to d-CDs in DCM caused a slight ~5 nm blue shift (Figure 4F) due to HBD enhancing K_{nr} . However, no significant change occurred upon the addition of H₂O due to DCM–H₂O immiscibility, maintaining emission at ~520 nm. Overall, EtOH/H₂O introduction to DCM caused negligible fluorescence changes and only minor CIE coordinate shifts (Figure 4D, E, and K and Figure S14).

Adding EtOH to a-CDs in DMF increased 300–420 nm emission but decreased 520–600 nm intensity with a slight blue shift. The surface state emission peak's relative intensity was higher in DMF/EtOH than in pure DMF, as EtOH shifted polarity dominance, enhancing surface state emission, while hydrogen-bonding interactions reduced overall fluorescence intensity (Figures 3H and 4G and I). H₂O addition enhanced the 420 nm emission and fully quenched 520–600 nm fluorescence (Figure 4H and I), as its stronger HBD ability suppressed deep defective/surface state but promoted intrinsic state emission. Notably, the molecular state peak showed minimal shift and slight intensity attenuation under solvent changes, indicating weak solvent effects on it. Thus, fluorescence stayed orange with EtOH but turned red with H₂O, with corresponding CIE coordinate shifts (Figure 4L).

The CDs exhibited solvatofluorochromic behavior, which facilitated their application in multilevel encryption. First, an integrated “AND” logic gate system was designed using d-CDs (Figure 5A). Blue fluorescence (output 1) required the simultaneous presence of both input 1 (365 nm) and input 2 (*n*-hexane), constituting the first gate (Figure 5B). Subsequently, the second gate generated green PL (output 2) when both input 3 (output 1) and input 4 (EtOH) were applied (Figure 5C). Furthermore, when input 5 (output 2) and input 6 (H₂O) were activated, output 3 produced purple PL (Figure 5D). Furthermore, we developed an ASCII conversion-based

encryption system employing a 4 × 8 matrix (Figure 5E and F and Figure S24 and Table S6), where green-yellow dots under UV illumination represented “1” and other emissions denoted “0”. The initial state and after EtOH addition produced incorrect codes “SCU-” and “scu-”. Subsequent H₂O addition converted the ASCII binary to decimal, yielding the correct code “206437”. Meanwhile, we developed a paper-based system via determinant theory (Figure 5G, H, and I and Table S8). After impregnating the filter paper with CDs in various solvents, constituting determinant A (value = 80) under UV irradiation. Subsequent EtOH addition, it became determinant B (value = 16). Finally, added H₂O to turn it into determinant C (value = −352). The absolute value of the product of these three determinants ($|A| \times |B| \times |C|$) produced the final encrypted password “450560”.

In summary, we have tailored two types of CDs via a one-step solvothermal method. Systematic characterizations revealed that the PL of d-CDs originates from three emission states (intrinsic, deep defective, and surface states), while a-CDs formed by electron-accepting PNDI cross-linked d-CDs exhibit additional molecular state emission through ICT. Moreover, the solvatofluorochromic mechanisms in various protic and aprotic solvents of the tailored CDs were systematically deciphered. Since solvent molecules interact only with surface functional groups, the intrinsic state emission remains unaffected, while polarity and hydrogen-bonding exert opposing effects on the deep defective state, surface state, and molecular state emissions. Enhanced polarity and HBA boost emission by suppressing non-radiative decays, whereas HBD promotes non-radiative pathways, leading to fluorescence quenching. Leveraging these exceptional solvent-responsive properties, we developed advanced dynamic encryption systems through: physical circuit-based logic gate encryption, mathematical algorithms for binary-decimal conversion and determinant encryption, and color-coding technologies for anticounterfeiting. Our work not only provides novel perspectives for understanding the structure-emission relationship but also pioneers their solvatofluorochromic mechanisms exploration, opening new avenues for practical applications in advanced encryption and anticounterfeiting

METHODS

Synthesis and Purification of CDs. A total of 3.25 g of NTCDA and 1.30 g of *o*-PDA were dissolved in 60 mL of DMF and sonicated for 30 min to yield a homogeneous solution, which was subsequently transferred to a 100 mL polytetrafluoroethylene-lined reactor and heated at 180 °C for a duration of 10 h. After cooling to ambient temperature, the resultant reaction solution was centrifuged at 10 000 rpm for 15 min, yielding a brown supernatant and a red precipitate. The brown supernatant was diluted with two volumes of deionized water, and then DMF was removed by rotary evaporation under reduced pressure to obtain a solid product, which was washed several times with deionized water. Meanwhile, the red precipitate collected from the bottom layer was washed repeatedly with ethanol. Finally, the products were dried in an oven at 50 °C to afford dark brown carbon dots (d-CDs) and red carbon dots (a-CDs).

Theoretical Calculation. All density functional theory (DFT) calculations were performed to verify the van der Waals forces and hydrogen bonding effects between the five solvent molecules (*n*-hexane, DCM, DMF, EtOH, and H₂O) and d-CDs. The structure optimization was carried out by Gaussian 09 software at the B3LYP-D3/6-31g** level with the IEFPCM implicit solvent model, while the calculation of the binding energy between molecules was performed at the B3LYP-D3/6-

311g** level. Meanwhile, the basis set superposition error (BSSE) was accounted for and corrected in the adsorption energy calculations. The grid data for the Independent Gradient Model based on Hirshfeld partition (IGMH) isosurface maps were computed using the Multiwfn software, followed by visualization with the VMD program.

Detailed material preparation and experimental procedures are described in the [Supporting Information](#).

■ ASSOCIATED CONTENT

SI Supporting Information

The Supporting Information is available free of charge at <https://pubs.acs.org/doi/10.1021/acs.nanolett.5c05189>.

Experimental details, materials and methods, including the synthetic procedures and characterization data for all compounds, relevant data for zeta potential, band gap energy, fluorescence spectroscopy, and encryption applications, and along with references (PDF)

■ AUTHOR INFORMATION

Corresponding Authors

Shuangquan Lai – School of Chemical Engineering, Sichuan University, Chengdu 610065, China; orcid.org/0009-0009-7150-8868; Email: shuangquanlai@scu.edu.cn

Yi Deng – School of Chemical Engineering and State Key Laboratory of Advanced Polymer Materials, Sichuan University, Chengdu 610065, China; Department of Mechanical Engineering, The University of Hong Kong, Hong Kong 999077, China; orcid.org/0000-0002-1765-5244; Email: dengyibandeng@scu.edu.cn

Authors

Shujing Wang – School of Chemical Engineering, Sichuan University, Chengdu 610065, China

Lei Rong – School of Chemical Engineering, Sichuan University, Chengdu 610065, China

Wenxuan He – School of Chemical Engineering, Sichuan University, Chengdu 610065, China

Yau Kei Chan – Department of Ophthalmology, The University of Hong Kong, Hong Kong 999077, China

Complete contact information is available at:

<https://pubs.acs.org/doi/10.1021/acs.nanolett.5c05189>

Author Contributions

Shujing Wang, Shuangquan Lai, and Yi Deng jointly conceived the concepts and designed the study. Shujing Wang developed materials and methods of fabrication, performed structural and fluorescence characterizations, and completed the cryptographic application demonstrations. Lei Rong, Wenxuan He, Yau Kei Chan, Shuangquan Lai, and Yi Deng provided suggestions on designing experiments and analyzing the results. Shujing Wang and Shuangquan Lai wrote the manuscript with input from all authors. Shuangquan Lai and Yi Deng supervised the study.

Funding

This work is jointly funded by the National Natural Science Foundation of China (22305098, 32571536, and 32271392), the Natural Science Foundation of Sichuan (2024NSFSC0676 and 2023NSFSC0333), the Sichuan University–Zigong Science and Technology Cooperation Funding (2024CDZG-24), the Fundamental Research Funds for the Central Universities, and the Sichuan University Postdoctoral Interdisciplinary Innovation Fund.

Notes

The authors declare no competing financial interest.

■ ACKNOWLEDGMENTS

The authors thank Wen Tian and Yanping Huang from the Center of Engineering Experimental Teaching, School of Chemical Engineering, Sichuan University, for their help with the FTIR. The authors thank Zhonghui Wang and Qingshuang Song (College of Biomass Science and Engineering, Sichuan University) for their help in UV–vis DRS and PL spectroscopy characterizations. The authors thank Shaolan Wang (Analytical & Testing Center, Sichuan University) for her help in TGA testing. The authors extend their gratitude to Jian Biao from Scientific Compass (www.shiyanjia.com) for providing invaluable assistance with the TEM analysis. The authors thank Ceshigo Research Service (www.ceshigo.com) for providing TA testing. The authors thank SuanChou (suan-chou.com) for the help in DFT calculations. We thank Dong Yu with Digital scanning system (WISLEAP WS-10), Linzhu Li with Digital scanning system (Olympus VS200) and Leica DMI 8 fluorescence microscope in Life Science Core Facilities (College of Life Sciences, Sichuan University). Thanks to eceshi (www.eceshi.com) for PL analysis.

■ REFERENCES

- (1) Arppe, R.; Sorensen, T. J. Physical unclonable functions generated through chemical methods for anti-counterfeiting. *Nat. Rev. Chem.* **2017**, *1*, 13.
- (2) Li, Z.; Liu, X.; Wang, G.; Li, B.; Chen, H.; Li, H.; Zhao, Y. Photoresponsive supramolecular coordination polyelectrolyte as smart anticounterfeiting inks. *Nat. Commun.* **2021**, *12*, 1363.
- (3) Shen, Y.; Le, X.; Wu, Y.; Chen, T. Stimulus-responsive polymer materials toward multi-mode and multi-level information anti-counterfeiting: recent advances and future challenges. *Chem. Soc. Rev.* **2024**, *53*, 606–623.
- (4) Shi, W.; Wang, R.; Liu, J.; Peng, F.; Tian, R.; Lu, C. Time-dependent Phosphorescence Color of Carbon Dots in Binary Salt Matrices through Activations by Structural Confinement and Defects for Dynamic Information Encryption. *Angew. Chem., Int. Ed.* **2023**, *62*, No. e202303063.
- (5) Ren, W.; Lin, G.; Clarke, C.; Zhou, J.; Jin, D. Optical Nanomaterials and Enabling Technologies for High-Security-Level Anticounterfeiting. *Adv. Mater.* **2020**, *32*, No. e1901430.
- (6) Larin, A. O.; Dvoretckaja, L. N.; Mozharov, A. M.; Mukhin, I. S.; Cherepakhin, A. B.; Shishkin, I. I.; Ageev, E. I.; Zuev, D. A. Luminescent Erbium-Doped Silicon Thin Films for Advanced Anti-Counterfeit Labels. *Adv. Mater.* **2021**, *33*, No. e2005886.
- (7) Xie, Y.; Zhao, X.; Wang, H.; Tian, Y.; Liu, C.; Wu, J.; Cui, J.; Zhou, Z.; Chen, J.; Chen, X. Hydrogen Bond-Associated Photofluorochromism for Time-Resolved Information Encryption and Anti-counterfeiting. *Angew. Chem., Int. Ed.* **2025**, *64*, No. e202414846.
- (8) Jiang, Y.; Ma, J.; Ran, Z.; Zhong, H.; Zhang, D.; Hadjichristidis, N. A Versatile Strategy for Multi-Stimuli-Responsive Fluorescent Material Based on Cross-Linking-Induced Emission: Applications in Encryption. *Angew. Chem., Int. Ed.* **2022**, *61*, No. e202208516.
- (9) Zhang, Y. Q.; Lu, S. Y. Lasing of carbon dots: Chemical design, mechanisms, and bright future. *Chem.* **2024**, *10*, 134–171.
- (10) Zhang, Y.; Liu, Y.; Ren, X.; Kang, Y.; Ding, S.; Lu, S. Adjusting TADF and Phosphorescence for Tailored Dynamic Time-Dependent Afterglow Colored Carbon Dots spanning Full Visible Region. *Angew. Chem., Int. Ed.* **2025**, *64*, No. e202421421.
- (11) Guan, S.; Chen, X.; Yu, R.; Xu, W.; Wu, Z.; Doug Suh, Y.; Liu, X.; Huang, W. Opal-Inspired SiO₂-Mediated Carbon Dot Doping Enables the Synthesis of Monodisperse Multifunctional Afterglow Nano-composites for Advanced Information Encryption. *Angew. Chem., Int. Ed.* **2025**, *64*, No. e202415632.

- (12) Zhu, S. J.; Song, Y. B.; Zhao, X. H.; Shao, J. R.; Zhang, J. H.; Yang, B. The photoluminescence mechanism in carbon dots (graphene quantum dots, carbon nanodots, and polymer dots): current state and future perspective. *Nano Res.* **2015**, *8*, 355–381.
- (13) Sun, Y. P.; Zhou, B.; Lin, Y.; Wang, W.; Fernando, K. A.; Pathak, P.; Mezziani, M. J.; Harruff, B. A.; Wang, X.; Wang, H.; Luo, P. G.; Yang, H.; Kose, M. E.; Chen, B.; Veca, L. M.; Xie, S. Y. Quantum-sized carbon dots for bright and colorful photoluminescence. *J. Am. Chem. Soc.* **2006**, *128*, 7756–7757.
- (14) Wang, X.; Cao, L.; Yang, S. T.; Lu, F.; Mezziani, M. J.; Tian, L.; Sun, K. W.; Bloodgood, M. A.; Sun, Y. P. Bandgap-like strong fluorescence in functionalized carbon nanoparticles. *Angew. Chem., Int. Ed.* **2010**, *49*, 5310–5314.
- (15) Zhu, S.; Meng, Q.; Wang, L.; Zhang, J.; Song, Y.; Jin, H.; Zhang, K.; Sun, H.; Wang, H.; Yang, B. Highly photoluminescent carbon dots for multicolor patterning, sensors, and bioimaging. *Angew. Chem., Int. Ed.* **2013**, *52*, 3953–3957.
- (16) Mondal, S.; Yucknovsky, A.; Akulov, K.; Ghorai, N.; Schwartz, T.; Ghosh, H. N.; Amdursky, N. Efficient Photosensitizing Capabilities and Ultrafast Carrier Dynamics of Doped Carbon Dots. *J. Am. Chem. Soc.* **2019**, *141*, 15413–15422.
- (17) Yang, H.; Liu, Y.; Guo, Z.; Lei, B.; Zhuang, J.; Zhang, X.; Liu, Z.; Hu, C. Hydrophobic carbon dots with blue dispersed emission and red aggregation-induced emission. *Nat. Commun.* **2019**, *10*, 1789.
- (18) Ji, C.; Zeng, F.; Xu, W.; Zhu, M.; Yu, H.; Yang, H.; Peng, Z. Hydrogen Bond-Mediated Self-Assembly of Carbon Dots Enabling Precise Tuning of Particle and Cluster Luminescence for Advanced Optoelectronic Applications. *Adv. Mater.* **2025**, *37*, No. e2414450.
- (19) Ai, L.; Xiang, W.; Xiao, J.; Liu, H.; Yu, J.; Zhang, L.; Wu, X.; Qu, X.; Lu, S. Tailored Fabrication of Full-Color Ultraprecise Room-Temperature Phosphorescence Carbon Dots Composites with Unexpected Thermally Activated Delayed Fluorescence. *Adv. Mater.* **2024**, *36*, No. e2401220.
- (20) Chen, Y.-J.; Zhang, J.-Z.; Wu, Z.-X.; Qiao, Y.-X.; Zheng, L.; Wondu Dagnaw, F.; Tong, Q.-X.; Jian, J.-X. Molecular Engineering of Perylene Diimide Polymers with a Robust Built-in Electric Field for Enhanced Solar-Driven Water Splitting. *Angew. Chem., Int. Ed.* **2024**, *63*, No. e202318224.
- (21) Yang, L.; Fu, Y.; Sun, F.; Deng, M.; Zhang, C.; Li, N.; Hao, D.; Wang, Q.; Zhuang, G. Preparation of novel diperylene-cored polyimide photocatalyst with broad-spectra response and high stability. *J. Colloid Interface Sci.* **2023**, *639*, 472–483.
- (22) Mintz, K. J.; Bartoli, M.; Rovere, M.; Zhou, Y. Q.; Hettiarachchi, S. D.; Paudyal, S.; Chen, J. Y.; Domena, J. B.; Liyanage, P. Y.; Sampson, R.; Khadka, D.; Pandey, R. R.; Huang, S. X.; Chusuei, C. C.; Tagliaferro, A.; Leblanc, R. M. A deep investigation into the structure of carbon dots. *Carbon* **2021**, *173*, 433–447.
- (23) Kato, T.; Yamada, Y.; Nishikawa, Y.; Ishikawa, H.; Sato, S. Carbonization mechanisms of polyimide: Methodology to analyze carbon materials with nitrogen, oxygen, pentagons, and heptagons. *Carbon* **2021**, *178*, 58–80.
- (24) Wang, B.; Wei, Z.; Sui, L.; Yu, J.; Zhang, B.; Wang, X.; Feng, S.; Song, H.; Yong, X.; Tian, Y.; Yang, B.; Lu, S. Electron-phonon coupling-assisted universal red luminescence of o-phenylenediamine-based carbon dots. *Light Sci. Appl.* **2022**, *11*, 172.
- (25) Yang, G. C.; Wu, C. L.; Luo, X. J.; Liu, X. Y.; Gao, Y.; Wu, P.; Cai, C. X.; Saavedra, S. S. Exploring the Emissive States of Heteroatom-Doped Graphene Quantum Dots. *J. Phys. Chem. C* **2018**, *122*, 6483–6492.
- (26) Al Kobaisi, M.; Bhosale, S. V.; Latham, K.; Raynor, A. M.; Bhosale, S. V. Functional Naphthalene Diimides: Synthesis, Properties, and Applications. *Chem. Rev.* **2016**, *116*, 11685–11796.
- (27) Koshkakar, G.; Klivansky, L. M.; Cao, D.; Snauko, M.; Teat, S. J.; Struppe, J. O.; Liu, Y. Alternative donor-acceptor stacks from crown ethers and naphthalene diimide derivatives: rapid, selective formation from solution and solid state grinding. *J. Am. Chem. Soc.* **2009**, *131*, 2078–2079.
- (28) Kelley, R. F.; Tauber, M. J.; Wasielewski, M. R. Intramolecular electron transfer through the 20-position of a chlorophyll a derivative: an unexpectedly efficient conduit for charge transport. *J. Am. Chem. Soc.* **2006**, *128*, 4779–4791.
- (29) Li, J.; Kang, M.; Zhang, Z.; Li, X.; Xu, W.; Wang, D.; Gao, X.; Tang, B. Z. Synchronously Manipulating Absorption and Extinction Coefficient of Semiconducting Polymers via Precise Dual-Acceptor Engineering for NIR-II Excited Photothermal Theranostics. *Angew. Chem., Int. Ed.* **2023**, *62*, No. e202301617.
- (30) Guo, D.; Hou, Y.; Xu, Q.; Wang, B.; Zhang, T.; Cheng, Q.; Chen, M.; Huang, L.; Xing, G.; Qu, S. J-type assembled Pt(IV)-coordinated carbon dots for near-infrared light-triggered pyroptosis. *Light Sci. Appl.* **2025**, *14*, 163.
- (31) Hu, X.; Zhu, C.; Sun, F.; Chen, Z.; Zou, J.; Chen, X.; Yang, Z. J-Aggregation Strategy toward Potentiated NIR-II Fluorescence Bioimaging of Molecular Fluorophores. *Adv. Mater.* **2024**, *36*, No. e2304848.
- (32) Würthner, F.; Kaiser, T. E.; Saha-Möller, C. R. J-aggregates: from serendipitous discovery to supramolecular engineering of functional dye materials. *Angew. Chem., Int. Ed.* **2011**, *50*, 3376–3410.
- (33) Lv, H.; Yao, Y.; Li, S.; Wu, G.; Zhao, B.; Zhou, X.; Dupont, R. L.; Kara, U. I.; Zhou, Y.; Xi, S.; Liu, B.; Che, R.; Zhang, J.; Xu, H.; Adera, S.; Wu, R.; Wang, X. Staggered circular nanoporous graphene converts electromagnetic waves into electricity. *Nat. Commun.* **2023**, *14*, 1982.
- (34) Pu, C.; Qin, H.; Gao, Y.; Zhou, J.; Wang, P.; Peng, X. Synthetic Control of Exciton Behavior in Colloidal Quantum Dots. *J. Am. Chem. Soc.* **2017**, *139*, 3302–3311.
- (35) Liu, Z.; Li, J.; Zhao, C.; Zhang, Z.; Wu, P.; Chen, J.; He, X.; Zhang, S.; Tian, Y. Molecular Engineering Enables Bright Carbon Dots for Super-Resolution Fluorescence Imaging and In Vivo Optogenetics. *Adv. Mater.* **2025**, *37*, No. e2410786.
- (36) Zhang, T.; Zhu, J.; Zhai, Y.; Wang, H.; Bai, X.; Dong, B.; Wang, H.; Song, H. A novel mechanism for red emission carbon dots: hydrogen bond dominated molecular states emission. *Nanoscale* **2017**, *9*, 13042–13051.
- (37) Liu, E.; Liang, T.; Ushakova, E. V.; Wang, B.; Zhang, B.; Zhou, H.; Xing, G.; Wang, C.; Tang, Z.; Qu, S.; Rogach, A. L. Enhanced Near-Infrared Emission from Carbon Dots by Surface Deprotonation. *J. Phys. Chem. Lett.* **2021**, *12*, 604–611.
- (38) Terenzi, F.; Painelli, A.; Katan, C.; Charlot, M.; Blanchard-Desce, M. Charge instability in quadrupolar chromophores: symmetry breaking and solvatochromism. *J. Am. Chem. Soc.* **2006**, *128*, 15742–15755.
- (39) Lekha, P. K.; Prasad, E. Tunable emission of static excimer in a pyrene-modified polyamidoamine dendrimer aggregate through positive solvatochromism. *Chemistry* **2011**, *17*, 8609–8617.
- (40) Reckmeier, C. J.; Wang, Y.; Zboril, R.; Rogach, A. L. Influence of Doping and Temperature on Solvatochromic Shifts in Optical Spectra of Carbon Dots. *J. Phys. Chem. C* **2016**, *120*, 10591–10604.
- (41) Basu, N.; Mandal, D. Solvatochromic Response of Carbon Dots: Evidence of Solvent Interaction with Different Types of Emission Centers. *J. Phys. Chem. C* **2018**, *122*, 18732–18741.